Physical Optics and Electronics

Academic and Research Staff
Professor Rajeev J. Ram, Dr. Xiaoyun Guo

Graduate Students
Reja Amatya, Harry Lee, Kevin Lee, Tom Liptay, Peter Mayer, Jason Orcutt, Tauhid Zaman

Technical and Support Staff
Catherine Bourgeois

Overview

The research in the Physical Optics and Electronics Group is divided along three primary themes:
- Integrated Photonics
- Biophotonics and Bioprocess
- Thermodynamics of Semiconductor Devices

In all three areas the goal of this research is to exploit processes in physics to invent new devices that lead to better systems. Each researcher works to model and design a new device, implement the design, and then integrated this device into a system which defines the state-of-the-art.

The major achievements of the laboratory during the last year were:
1. Demonstration of microbial cell growth in a microscale bioreactor to 5 times higher cell density than previously achieved.
2. First parallel cell culture experiment for a microscale bioreactor.
3. Demonstration of a polymer backplane for fluorescence based sensing
4. First demonstration of Faraday rotation in a fully-confined semiconductor waveguide
5. First high-resolution thermal images of a thermoelectric device under operation
6. Record high power density from a thin film thermoelectric power generator
7. First measurement of of dynamic range in a Ge on Si photodetector.

Microbial Growth in Parallel Integrated Bioreactor Arrays

Sponsor
DuPont MIT Alliance

Project Staff
Harry Lee, Professor Rajeev J. Ram
Paolo Boccazzi, Professor Anthony J. Sinskey

Bioprocesses with microbial cells play an important role in producing biopharmaceuticals such as human insulin and human growth hormone, and other products such as amino acids and biopolymers. Because bioprocesses involve the complicated interaction between the genetics of the microorganisms and their chemical and environmental conditions, hundreds or thousands of microbial growth experiments are necessary for to develop and optimize them. In addition, efforts to develop models for bioprocesses also require numerous growth experiments to study microorganism phenotypes.

We have designed and developed integrated arrays of microbioreactors that can provide the oxygen transfer and control capabilities of a stirred tank bioreactor in a high-throughput format. The devices comprise a novel peristaltic oxygenating mixer and microfluidic injectors (Fig. 1), which are fabricated using a process that allows combining multiple scale (100µm-1cm) and multiple depth (100µm-2mm) structures in a single mold. The microbioreactors have a 100µL working volume, a high oxygen transfer rate ($k_La \approx 0.1s^{-1}$), and closed loop control over dissolved oxygen and pH (±0.1). Overall, the system supports eight simultaneous batch cultures, in two parallel arrays, with two dissolved oxygen thresholds, individual pH set points, and automated near real-time monitoring of optical density, dissolved oxygen concentration, and pH.

These capabilities allowed the demonstration of multiple *Escherichia coli* aerobic fermentations to high cell densities (>12g-dcw/L, Fig. 2), with individual bioreactor performance on par with bench scale stirred tank bioreactors. The successful integration of diverse microfluidic devices and optical sensors in a scalable architecture opens a new pathway for continued development of parallel bioreactor systems.
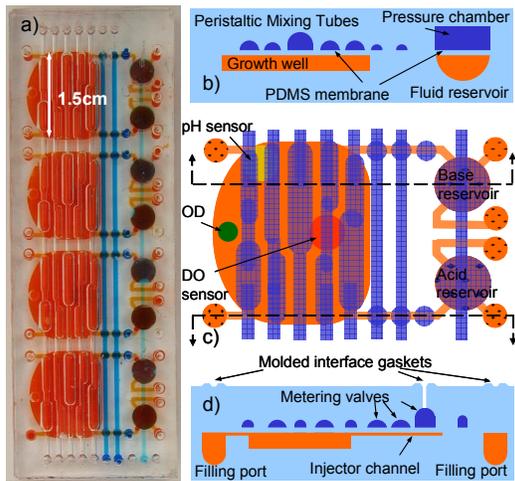
Fig. 1 Photograph and schematic of Parallel Integrated Bioreactor Array device. a) Photograph of four reactors integrated into a single module. b) Cross-section showing peristaltic oxygenating mixer tubes and fluid reservoir with pressure chamber. c) Top view of schematic showing optical sensors and layout of peristaltic oxygenating mixer and fluid injectors. d) Cross-section showing the fluid injector membrane pinch valves.
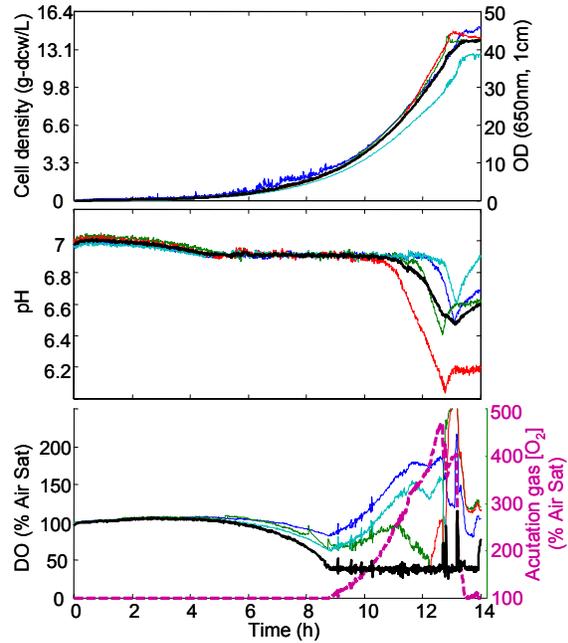
Fig. 2 Data from four *E. coli* fermentations on defined medium performed in a single microbioreactor array module. The heavy black line indicates the mean of the cell density and pH replicates, and the minimum of the dissolved oxygen replicates. The pH is controlled at 6.9 until approximately 10 hours when the base reservoirs were depleted. Due to slight differences in the $k_L a$, the oxygen concentration in three of the reactors did not remain near the set point. The oxygen concentration of the mixer actuation gas (bold magenta dashes), estimated from the duty cycle of the gas mixer switch, is shown by the orange dashed line and approximately follows the exponential growth of the cells.

Polymer Waveguides for Integrated Biosensors

Sponsor
DuPont MIT Alliance
NSF Center for Materials Science and Engineering

Project Staff
Kevin Lee, Professor Rajeev J. Ram

Fluorescence based sensors are used for determining environmental parameters such as dissolved oxygen or pH in biological systems. Such optical sensing techniques can provide real time monitoring capabilities without disturbing a biological system's equilibrium. Recently, there has been a drive to provide biological analysis tools in a compact form, usually resulting in arrays of miniature devices which can perform multiple functions or operations in parallel such as bacteria cultures, cell counting, or DNA analysis [1,2,3]. As these new types of chips become more integrated and parallel, the number of sensors required increases, which leads to an increase in the size and complexity of off-chip detection systems.

In an effort to simplify and integrate the detection side of these systems, a platform is being developed which utilizes the same polymer materials used for these chips to create waveguide based optical components. Since collected signal intensity is a major concern in fluorescence collection systems, integrated waveguides must be large core (1 mm diameter) and large NA (0.62), depending on the distance between the waveguide and the fluorescence source.

To overcome the challenge of fabricating large dimension waveguides with optical quality surfaces, a conventional fabrication approach using plastics is utilized over a microfabrication approach generally used for microfluidics. While conventional milling can easily create structures with dimensions of 1 mm, roughness from the fabrication process leads to diffuse surfaces and variations greater than 1 μm. To overcome the roughness due to milling and ultimately create large features with optical quality roughness, a solvent vapor polishing process is used where a solvent vapor such as methylene chloride vapor is used to liquefy the plastic surface [4]. The degree of polishing can be controlled by varying the solvent pressure or also by varying the exposure time. Under optimal polishing conditions, the average roughness from sanded polycarbonate samples can be reduced from 1000 nm to 70 nm. By combining vapor polishing with CNC milling, CNC milling becomes a viable process for both optical and microfluidic master mold fabrication.

After mold fabrication, standard soft lithography processes are used to create negative PDMS replicas of the polycarbonate molds. In addition, PDMS molds are subject to e-beam deposition of evaporated silver to provide reflective surfaces where necessary. The same fabrication process is used for both waveguides and microfluidic components of the chip and the final oxygen sensing device is shown in Figure 1. The oxygen sensors used for this experiment are created by a mixture of Platinum(II) octaethylporphine ketone (PtOEPK) [5] and polystyrene deposited on glass disks. This fluorescent dye has a maximum absorption at 592 nm and emits at 759 nm.

Fabricated waveguides exhibit a propagation loss of 0.136 dB/cm at 626 nm and a measured 50% intensity numerical aperture of 0.5. E-beam deposited silver on PDMS measured a reflectivity of 72% with a HeNe laser at 632 nm. The design of the waveguide array is based on oxygen sensor locations within the parallel microbioreactor chip [2]. Compatibility of the optical backplane with measurements performed in the microbioreactor chip is demonstrated through dynamic oxygen measurements within a flowing channel of deoxygenated water. The experimental setup for measuring oxygen concentration consists of four modulated LEDs coupled to input guides through multimode fibers and four photodetectors, one placed at each output guide to collect fluorescence. The oxygen sensors function by measuring the phase shift resulting from a decrease in fluorescence lifetime of PtOEPK dye in the presence of oxygen. Each sensor measures a maximum phase change of 30 degrees with a standard deviation of 0.5 degrees from

nitrogen to air. The change in oxygen concentration for the flowing system due to oxygen diffusion through PDMS measured by the four different sensors is shown in Figure 2. The demonstration of simultaneous and independent measurements of oxygen concentration at four different locations within a dynamic system shows the effectiveness of a waveguide system at performing optical measurements within a microfluidic chip in a compact form.
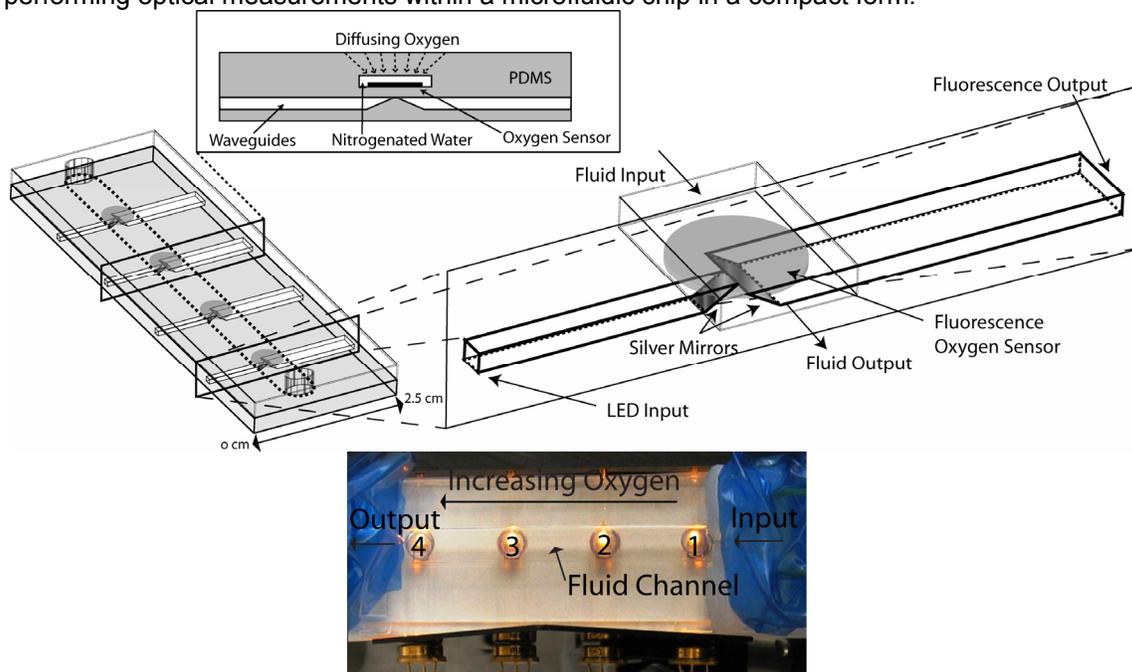
Figure 1. A schematic of the integrated fluidic and photonic device showing the device and a cross sectional view. Fluorescence based oxygen sensors at the base of the fluidic channel lie on a plane sitting above the collection and excitation optics. A picture of the fabricated optical and fluidic integrated device is shown.
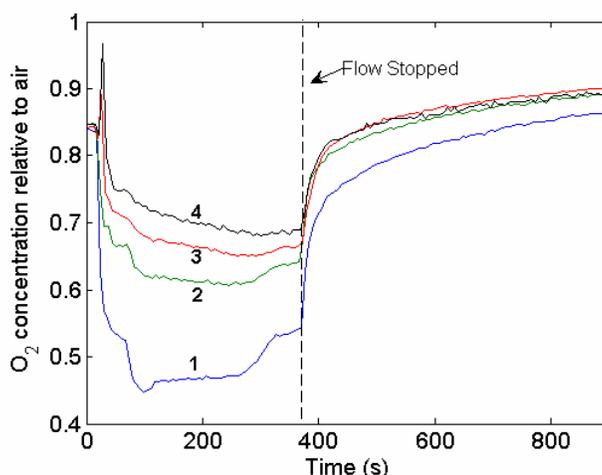
Figure 2. Sensors 1-4 are placed with even spacing along the channel. Deoxygenated water is flowed through the channel at 0.5 ml/min starting at 38 seconds. Diffusion of oxygen through PDMS is measured during flow as well as with flow off. Measurements during flow show similar diffusion behavior as measurements taken while flow is stopped.

[1] T. Vilkner, D. Janasek, A. Manz, "Micro Total Analysis Systems. Recent Developments," Anal. Chem. **76**, 3373-3386 (2004).
[2] H. L. T. Lee, R. J. Ram, "Integrated Fluid Injectors and Mixers for pH Control in Miniature Bioreactor Arrays," Proc. MicroTAS conference 2005 **v 1**, p. 34-36 (2005)
[3] L Cui, T Zhang, H Morgan, "Optical particle detection integrated in a dielectrophoretic lab-on-a-chip," J. Micromech. Microeng. **12**, 7-12 (2002)
[4] V. D. McGinniss, "Vaporous Solvent Treatment of Thermoplastic Substrates," United States Patent 4529563 (1985)
[5] Dmitri B. Papkovsky, "Phosphorescent Complexes of Porphyrin Ketones: Optical Properties and Application to Oxygen Sensing," Anal. Chem. **67,** 4112-4117 (1995).

Linewidth and Stokes shift of Colloidal Nanoparticles

Sponsors
Packard Foundation
Center for Materials Science and Engineering (NSF-MRSEC)

Project Staff
Tom Liptay, Professor Rajeev J. Ram

We investigate the size dependence of the room temperature homogeneous linewidth and Stokes shift for CdSe/CdS/ZnS nanocrystals (NCs). The room temperature homogeneous linewidth is an important parameter because it sets a fundamental limit on how narrow the ensemble photoluminescence (PL) spectra can be made which is important for many applications – optical barcodes, flat panel displays, biological imaging, etc. We measure the ensemble PL and absorption spectra of high quality CdSe/CdS/ZnS NCs in polymer (PLMA) as a function of size (R=1.5-4nm) and temperature (5-300K).

We extract a homogenous linewidth from our PL spectra using a deconvolution procedure assuming that the homogeneous spectrum is either a Lorentzian or a Gaussian. The dominant mechanisms of homogeneous broadening at room temperature (RT) are expected to be acoustic and optical phonon scattering. Acoustic phonon broadening is expected to scale like $1/R^2$ and have a Gaussian spectrum. Optical phonon broadening is expected to scale like R and has a Lorentzian spectrum in bulk CdSe. Our implied homogenous linewidth linewidth has an approximate $1/R^2$ dependence for small R and the Gaussian fit agrees well with what is expected theoretically for a CdSe NC in an SiO_2 matrix. [1] The linewidth increases for our largest sample and the Lorentzian fit approaches what is expected for bulk CdSe at room temperature.

The same acoustic phonon scattering model that explains the homogeneous linewidth can explain most of the Stokes shift. The figure shows 4 contributions to the Stokes shift. Acoustic and optical phonon scattering are the 2 dominant mechanisms in our model. The fine structure contribution originates from the fact that higher energy levels of the bandedge exciton have a higher oscillator strength than lower energy levels. As a result, the higher levels dominate the absorption spectrum, while the emission tends to come from the lower energy levels (since they are more populated assuming a Boltzmann distribution). The inhomogeneous contribution comes from the fact that larger NCs have a larger cross section and hence absorb more of the excitation in photoluminescence (PL) experiments. Previous explanations of the Stokes shift assumed the oscillator strengths were different for absorption and emission, which is hard to justify physically. Our model assumes that the oscillator strengths are the same for absorption and emission and can also explain most of the temperature dependence of the ensemble linewidth.
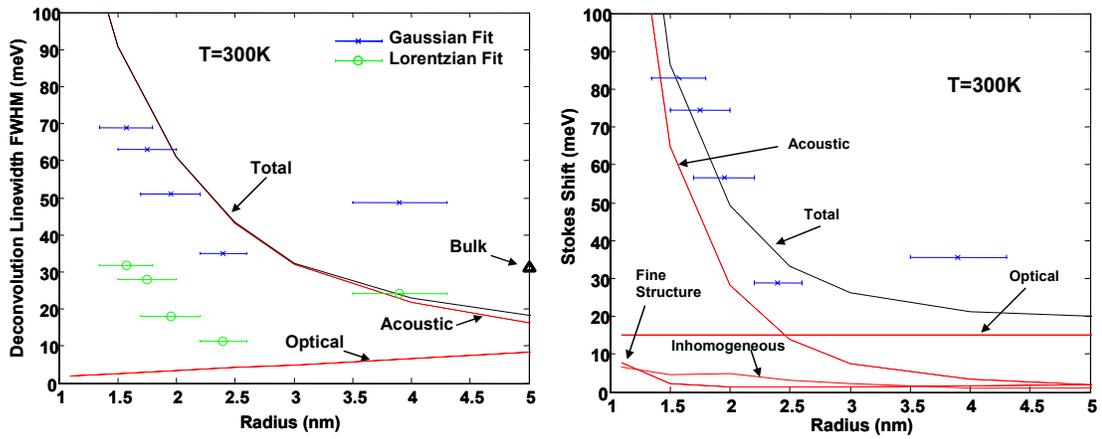
Figures: Left - Predicted temperature dependence of the homogeneous linewidth from [1] and our experimentally extracted linewidths assuming either a Gaussian or Lorentzian homogeneous spectrum. Right – Predicted Stokes shift using theory from [1] and our measured values.

[1] Goupalov, S. V., R. A. Suris, et al. (2001). "Homogeneous broadening of the zero-optical-phonon spectral line in semiconductor quantum dots." <u>Nanotechnology</u> **12**: 518-522.

Faraday Rotation in InP Waveguide Devices

Sponsor
DARPA

Project Staff
Tauhid Zaman, Dr. Xiaoyun Guo, Professor Rajeev Ram

The demonstration of waveguide isolators and circulators that can easily be integrated with active and passive optical components is essential to large scale photonic integration. Not only do these components provide functionality that cannot be achieved in integrated circuits today, but they also enable complex photonic circuit design by isolating or 'buffering' the various parts of a circuit. We have demonstrated that Faraday rotators – a central component in bulk isolators and circulators – can be fabricated from Fe:InP and Fe:InGaAsP.

Realization of integrated Faraday rotators requires that magneto-optical materials be incorporated into a waveguide where TE and TM modes have nearly equal propagation constants [1]. The width of high-mesa waveguides can be etch-tuned to achieve zero birefringence [2]. The waveguides used here are high-mesa structures consisting of a 0.5 μm Fe:In$_{1-x}$Ga$_x$As$_y$P$_{1-y}$ (x=.290 and y=.628) core layer and 1.0 μm Fe:InP cladding layers. The Fe doping in the core of the measured waveguides is 8.0 x 10^{16} cm^{-3}. Waveguides of different widths were fabricated with low pressure methane based reactive ion etching. The waveguide width for zero-birefringence at a wavelength of 1.55 μm is 1.4 μm [3].

To measure the waveguide Faraday rotation, a spinning magnet with an oscillating 30 mT magnetic field was used. The waveguides fabricated did not achieve zero-birefringence, mainly due to fabrication errors in the width. The birefringence of the waveguide suppresses the Faraday rotation and produces an oscillatory behavior as the wavelength is changed. To extract the Verdet coefficient, which indicates the strength of the Faraday rotation, for a zero-birefringence waveguide in this material, simulations of the waveguide Faraday rotation were run with the Verdet coefficient used as a fitting parameter. Fig. 1 shows the experimental results compared to the simulation results for a 1.8 μm wide waveguide. The rapid oscillations are due to cavity enhanced Faraday rotation and the slower oscillation is due to the wavelength dependent birefringence. As can be seen, the measured Faraday rotation exhibits an oscillatory behavior as expected from theory.

The Verdet coefficient of the waveguide Faraday rotation simulations was adjusted to match the experimental data. Fig. 2 shows the peak amplitude of the Faraday rotation in the wavelength range 1.52 μm to 1.60 μm as a function of waveguide width for different values of the Verdet coefficient. The three large circles on the graph represent the experimental results for the peak amplitude of the rotation. From this graph it can be seen that the Verdet coefficient of the waveguides is 33.3 °/mm/T. A 45° rotation could be obtained in an Fe:InGaAsP waveguide only a few millimeters in length. For comparison, YIG, which is used in bulk isolators, has a Verdet coefficient of 130 °/mm/T. These measurements show that InP based waveguide Faraday rotators can be achieved with a rotational power about one fourth as strong as commercial Faraday rotators.

The Faraday rotation in these waveguides can be further enhanced using two different techniques. First, using a material with a bandgap closer to the operational wavelength will increase the Faraday rotation [4]. This can be achieved by adjusting the composition of the InGaAsP core. Second, increasing the magnetic dopant concentration will increase the Faraday rotation [5]. By using these techniques to improve the waveguide Faraday rotators, the achievement of monolithically integrated optical isolators and circulators will be made possible.
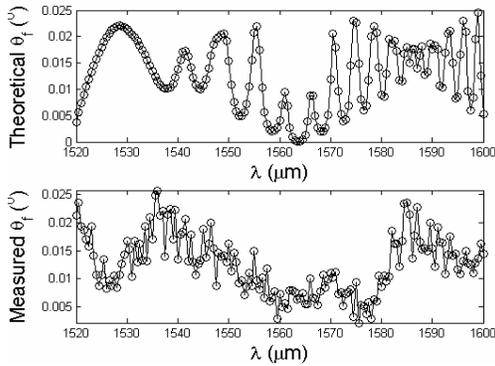
Fig. 1. Theoretical and experimental Faraday rotation for 1.8 μm wide waveguide. The waveguide length is 1.32 mm and the Faraday rotation coefficient is 1°/mm for the theoretical rotation. The magnetic field strength is 30 mT for the measured rotation.
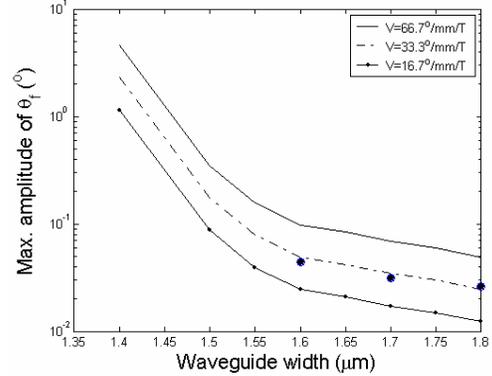
Fig. 2. Amplitude of Faraday rotation oscillation in wavelength range 1.52 μm to 1.60 μm vs. waveguide width. The waveguide length is 1.32 mm and the applied magnetic field is 30 mT. The three large circles represent experimental data and the lines represent simulation.

References

1. R. Wolfe, J. Hegarty, J. F. Dillon, Jr., L.C. Luther, G.K. Celler, L. E. Trimble and C. S. Dorsey, "Thin-film waveguide magneto-optic isolator," Appl. Phys. Lett. **46**(9), pp. 817-819, 1985.
2. M. Kohtoku, H. Sanjoh, S. Oku, Y. Kadota, and Y. Yoshikuni, "Polarization independent semiconductor arrayed waveguide grating using a deep-ridge waveguide structure," *IEICE Trans. Electron.*, vol. E81-C, no. 8, pp. 1195-1204, 1998.
3. X. Guo, T. Zaman, R. J. Ram, "Magneto-Optical Semiconductor Waveguides for Integrated Isolators," *Proc. SPIE,* 2005, vol. 5729*,* p. 152-159*.*
4. L. Roth, "Theory of Faraday Effect in Solids," *Phys. Rev.*, vol. 133, pp. A542-A553, January 1964.
5. C. Chen, R. Wang, X. Wang, and K. Ma, "Giant Faraday rotation in diluted magnetic semiconductor $Cd_{1-x}Fe_xTe_x$," *Solid State Commun.*, vol. 92, pp. 725-729, December 1994.

## Nanoscale Thermal Imaging Microscopy of Thermoelectric Devices

Sponsors
Office of Naval Research
DARPA

Project Staff
Peter Mayer, Professor Rajeev J. Ram

In many solids, a change in temperature produces a small change in the dielectric response of the material, and particularly in the index of refraction. By measuring the change in reflectance from a device or material whose temperature is modulated in some way, an image of the temperature change can be obtained, after proper calibration. This approach is useful for examining heat transport in electronic/optoelectronic devices, since the heating due to a changing bias current or voltage can be measured. And unlike typical (infrared) thermal imaging, deep sub-micron spatial resolution is possible. Shown below in Fig.1 are (uncalibrated) thermoreflectance images of the Joule and Peltier heating and cooling in a 4.9 μm thick InGaAs-based superlattice incorporating semimetallic self-assembled ErAs nanodots, on an InP substrate. The ErAs dots and the superlattice both scatter phonons participating in cross-plane heat transport, reducing the thermal conductivity to below the alloy limit by nearly a factor of two. The dots and the superlattice are also expected to increase the free electron concentration, the electrical conductivity, and the Seebeck coefficient.

The thermal imaging technique used here relies on a CCD camera triggered 4 times per temperature cycle and averaged over many cycles, so that each pixel of the camera functions as a lock-in detector. Because the change in reflectance is small (e.g. 1 part in 10000, per degree Kelvin) it has been suggested that the temperature resolution of the technique is limited by the least significant bit size of the quantizer of the CCD array, giving rise to a minimum temperature resolution in the single Kelvin range. But due to the presence of noise in the pre-quantized signal, the resolution can actually be improved considerably by sufficient averaging. We have demonstrated a temperature resolution on the order of 10 mK and developed a quantitative theory describing the statistics and accuracy of the measurement, set by the noise characteristics of the camera and the measurement characteristics. Fig. 2 shows the measurement of a temperature signal smaller than that corresponding to the bit size of the CCD array, as a function of the measurement duration. The theoretically predicted mean and standard deviation are close to those measured.
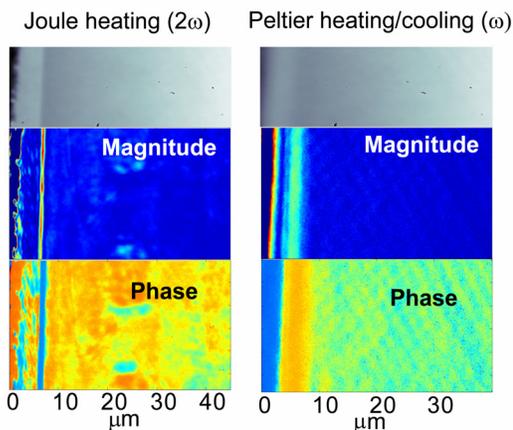
Figure 1. Cross-plane magnitude and phase images of the Joule and Peltier contributions to the thermal response in a nanostructured thermoelectric element. Superlattice (clearly visible in the top photomicrographs) is to the left of the image.
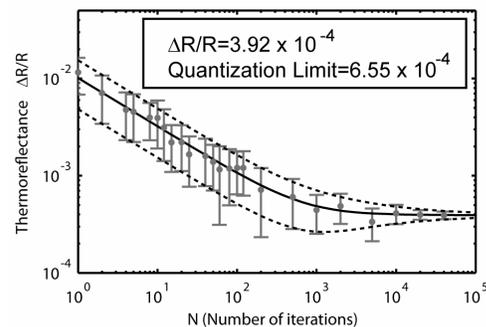
Figure 2. Measurements (gray) and theory (black) for sub-quantization thermoreflectance measurements. The measurement converges for sufficient iterations (long enough duration).

Demonstration of High Power Density Thermoelectric Generation

Sponsors
Office of Naval Research

**Project Staff**
Peter Mayer, Professor Rajeev J. Ram

Thermoelectric power generation relies on the Peltier/Seebeck effects to convert heat power into electrical power quietly and with no moving parts. Recently, significant improvements have been made in the material parameters of thermoelectric (TE) elements using nanostructured growth techniques. Heterostructures, quantum confinement, and embedded nanoparticles have been suggested as a means to substantially increase the Seebeck coefficient and electrical conductivity and decrease the thermal conductivity relative to that of bulk materials. Fig.1 shows a material designed to enhance thermoelectric performance by incorporating self-assembled ErAs nanodots into an InGaAs matrix.

However, thin-film devices under strongly non-equilibrium conditions (large temperature gradients, large generated current densities) have proven difficult to measure and apply practically, particularly in the cross-plane (growth) direction. The small impedance and the large influence of electrical and thermal parasitics complicate the use and characterization of individual elements. Also, many TE thin-films are grown on substrates and separating the effects of the thin-film from those of the substrate is difficult. Maintaining a large temperature difference across a thin-film in the cross-plane direction requires that a correspondingly large heat flux be removed at the cold side of the element.

Provided these issues are addressed, single element measurements in strongly non-equilibrium conditions can provide information unavailable from wafer-level measurements, since the spatial and temperature variation of the material parameters within the superlattice can have large effects on performance, as can electrical parasitic resistances associated with transport through the multilayer structure. The measurements shown in Fig. 2 depict a test of the ErAs nanodot material under conditions similar to those expected in a real power generation application. The maximum power density generated here (6 W/cm^2) is several times that expected from a conventional optimized bulk material (e.g. Bi_2Te_3).
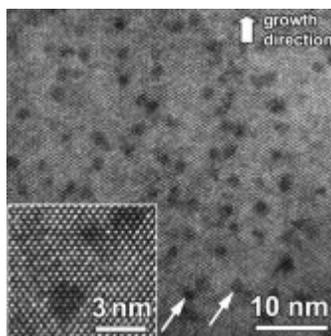
Figure 1. Cross-sectional SEM image of ErAs nanodots in InGaAs [from Zide et al., App. Phys. Lett. **87**, 112102 (2005)].
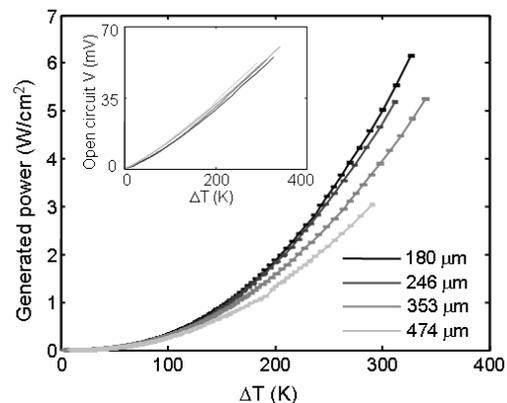
Figure 2. Measurements of the power density and open circuit voltage from single ErAs nanodot superlattice samples on varying length substrates, for large applied temperatures.

## Dynamic Range of Strained Ge-on-Silicon Photodetectors

Sponsors
DARPA

Project Staff
Jason Orcutt, Professor Rajeev J. Ram
Oluwamuyiwa Olubuyide, Professor Judy Hoyt

As photonic integrated circuits gain maturity in the silicon material system, new applications that require photonic components integrated with silicon electronic circuitry become possible. One such new application is the hybrid photonic-electronic analog-to-digital converter in which the sampling front end is achieved optically and the digital conversion back end is achieved electronically [1]. To allow this converter to achieve a high effective number of bits (ENOBs), an important figure-of-merit for these systems, photodetectors with a high dynamic range that are compatible with an integrated CMOS platform are necessary.

One such photodiode under development is fabricated in a germanium-on-silicon material system that is CMOS compatible. To characterize the linearity, we measured the spur-free dynamic range (SFDR) of the diodes using the test setup shown in Figure 1. To calculate the SFDR, the spectrum of the photodiode response to a two-tone RF-modulated input is measured as a function of modulation amplitude. As shown in the microwave spectrum analyzer screen inset to Figure 1, third-order nonlinearities produce in-band intermodulation distortion products (IMD3) that limit the dynamic range of the detector.

To ensure that observed nonlinearities are caused by the diodes, the output of the link laser was examined by using a lightwave front-end to the microwave spectrum analyzer and by replacing the Ge photodiodes with industry-standard Epitaxx InGaAs p-i-n photodiodes designed for CATV applications. To complete the data required to calculate SFDR, the noise floor of the link was measured, roughly integrating over a 2-GHz bandwidth with the microwave spectrum analyzer. This data and the calculated SFDR are shown in Figure 2. The demonstrated 34-dB SFDR of this link would currently allow for 5.6 effective bits if it was the limiting factor in the converter's performance.
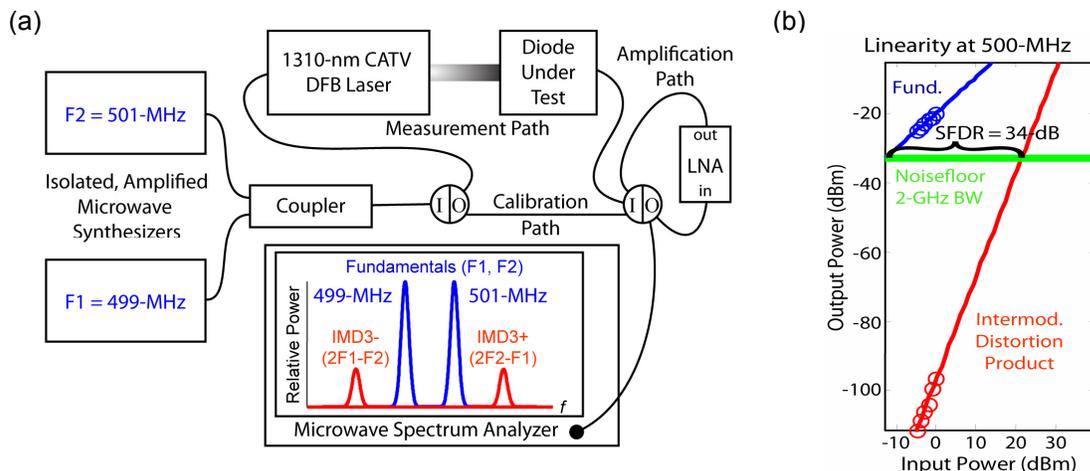
Figure 1: (a) Diagram showing the SFDR measurement setup. The block labeled LNA in the amplification path is a Miteq low-noise amplifier. (b) Spur-free dynamic range measurement on a 100x100 m Ge photodiode. The diode was biased at -3V in this measurement.

[1] Kärtner, F. X., et al. "Electronic Photonic Integrated Circuits for High Speed, High Resolution, Analog to Digital Converstion," *Proceedings of SPIE*, vol. 6125, 612503, 2006.

## Design and Measurement of Thermo-optics on Silicon

Sponsors
DARPA

Project Staff
Reja Amatya, Professor Rajeev J. Ram

The vision of optoelectronics started with integration of optics and electronics on the same substrate.. Electrical integrated circuits (IC) have been very successful on silicon substrate. Thus, silicon is one of the more desirable material for optoelectronic devices. Silicon (Si) as well as silicon nitride (SiN) optical waveguides are becoming integral components for optical systems because of their advantages of high index contrast and compatibility with IC.

Thermally tunable optical ring resonators made of SiN on silicon can be used as switches and filters. A small ring diameter (≈20 μm) allows large free spectral range. The temperature dependence of refractive index i.e. the thermo-optic effect of the core and cladding is utilized to tune these ring resonators. Resistive heaters are designed to sit on top of the cladding for thermal tuning. One of the key aspects while designing the heaters is minimum power dissipation per GHz in terms of tuning flexibility. Figure 1 shows a thermal simulation for a heater over a two ring filter.

Waveguides formed on silicon-on-insulator can have submicrosecond switching capabilities. These waveguides are heated by passing current through them and it is important to be able to study and measure the thermal characteristics of the device. Thermoreflectance spectroscopy is one of the many ways of measuring the device temperature. A temperature profile for a silicon waveguide of 0.5 μm thickness is shown by measuring the reflectance changes due to modulating current. Figure 2 shows the image of the melt waveguide along with temperature profile and the thermoreflectance image. The figure on the left inset shows the non-uniform temperature distribution within the waveguide. For the silicon melt waveguide, the measured thermo-optic coefficient (κ) was 1.1E-4/K which is similar to the reported values for silicon for the specific wavelength (510 nm). Similar measurements can be done on SiN ring resonators to obtain thermo-optic coefficient.
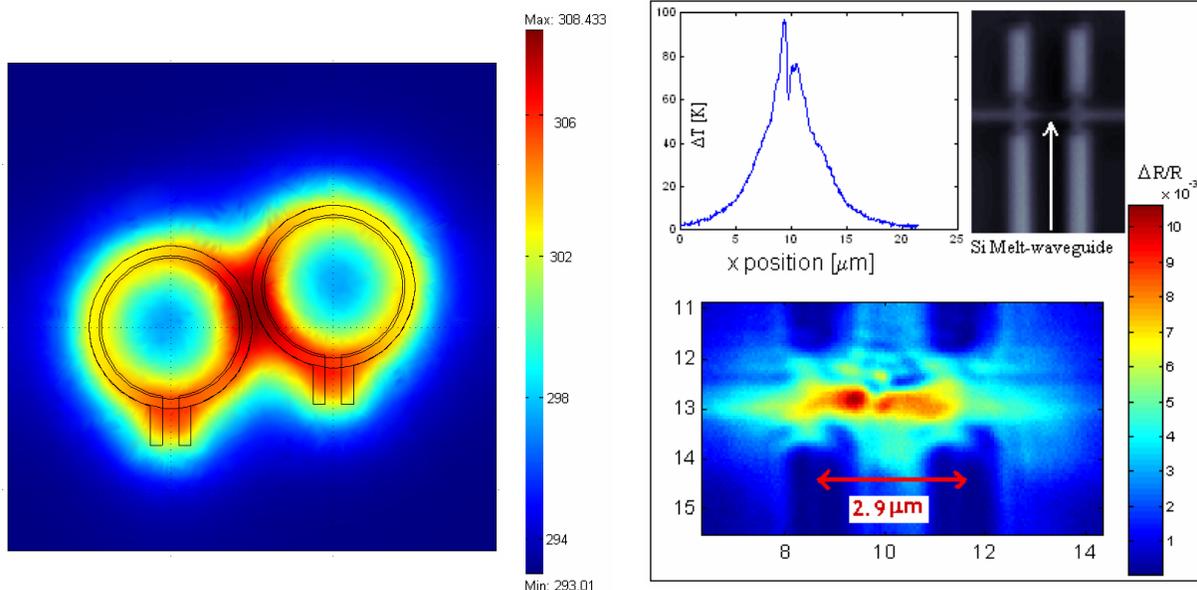
Figure 1: Temperature profile for thermal tuning of ring resonator.

Figure 2: Silicon melt waveguide thermal profile using thermoreflectance technique.